PHYSICAL REVIEW B **109**, 224419 (2024)

Soft magnons in van der Waals multiferroic NiI$_2$

Andi Cong and Ka Shen[*]
The Center for Advanced Quantum Studies and Department of Physics, Beijing Normal University, Beijing 100875, China and Key Laboratory of Multiscale Spin Physics, Ministry of Education, Beijing Normal University, Beijing 100875, China

(Received 20 March 2024; accepted 4 June 2024; published 13 June 2024)

The ferroelectric polarization in van der Waals multiferroic NiI$_2$ is believed to be induced by the helimagnetic spin order. The formation of the helimagnetic ground spin configuration and the properties of its spin excitation are yet to be clarified. In the present work, we explore the proper magnetic ground states with well-defined magnon spectra in a single-layer NiI$_2$, by analyzing the role of different interactions. While the spin frustration due to the ferromagnetic and antiferromagnetic exchange terms stabilizes a helimagnetic phase, the anisotropic Kitaev interaction introduces a canting of the spin rotation plane. We find the modulation vector of the helimagnetic structure can be continuously oriented within the atomic plane by the competition between the Kitaev interaction and the third-nearest-neighbor exchange. The calculation of magnon spectrum reveals anomalous features with soft magnons at finite wave vectors, which is found to be related with the vibration of the canting plane. From the finite-temperature calculation of the magnon spectra, we predict a magnetic phase transition driven by soft magnons, which cause a spatial modulation of the canting plane. Furthermore, a sign change is predicted in the temperature dependence of the transverse magnon thermal conductivity. Our results provide a comprehensive understanding of the spin ground state and the soft magnons in the van der Waals NiI$_2$.

DOI: 10.1103/PhysRevB.109.224419

I. INTRODUCTION

Since the invention of the mechanical exfoliation technique in 2004 [1], the two-dimensional (2D) materials have been intensively explored [2–7], where various outstanding advantages, such as high carrier mobility [1,8], superior thermal conductivity [9,10], and excellent optical transparency [11–13], have been demonstrated. The experimental achievement of 2D van der Waals (vdW) materials with intrinsic magnetism in 2017 [14,15] arouses great interests in investigating and seeking for the potential applications of 2D magnetic materials, whose magnetic properties can be efficiently manipulated via electrostatic doping [16,17], electrical field [18,19], and external strain [20]. Meanwhile, the 2D ferroelectricity in vdW materials, which hosts a switchable intrinsic ferroelectric polarization, has also garnered significant attention [21,22] as a promising candidate in information storage memory [23,24], ferroelectric-based topological devices [25], etc. As a hybrid of magnetism and ferroelectricity [26], 2D multiferroic materials, if accessible, may provide new opportunities to realize multifunctional devices [27,28].

Since the early study in 1950s [29], various bulk multiferroic materials have been discovered [30,31], such as BiFeO$_3$ [32–35], BiMnO$_3$ [36], Pb(Fe$_{1/2}$Nb$_{1/2}$)O$_3$ [37,38], and TbMnO$_3$ [39–42]. While type-I multiferroic is commonly referred to the multiferroic materials with different ferroic orders disentangled from each other, the ferroelectric polarizations in type-II multiferroic are induced by specific magnetic textures through the inverse Dzyaloshinskii-Moriya (DM) mechanism [43,44], the spin-dependent p-d hybridization [45,46], or the exchange striction [47]. The correlation between spin and electric polarization order in type-II multiferroic materials leads to a strong magnetoelectric coupling, which allows the electrical control of the magnetic moments as well as the manipulation of ferroelectric polarizations by a magnetic field. Among the type-II multiferroics, the NiI$_2$ with weak vdW coupling between atomic layers is regarded as a promising candidate for 2D multiferroic materials [48–53].

Bulk NiI$_2$ belongs to the space group $R\bar{3}m$ (point group D_{3d}) with the magnetic ions Ni^{2+} in each atomic layer forming a triangular lattice and different layers stacking in a rhombohedral structure [54]. The ferroelectric polarization in NiI$_2$ is believed to be induced by the spiral magnetic order through inverse DM mechanism [54]. As the temperature decreases from ambient temperature, bulk NiI$_2$ first undergoes a magnetic phase transition from the paramagnetic phase to the interlayer antiferromagnetic phase with a ferromagnetic order in each layer, followed by another transition to the helimagnetic phase [54–57]. The two transition temperatures were found to be $T_{\mathrm{N},1} \simeq 76$ K and $T_{\mathrm{N},2} \simeq 59.5$ K, respectively, at normal pressure and can be significantly elevated under high pressures [58]. In the helimagnetic phase, the spins of Ni^{2+} within a single layer form a canted proper screw (CPS) order with a period $\lambda \approx 7a$ along $[1\bar{1}0]$ direction, where a is the lattice constant, and a canting angle of $55 \pm 10^\circ$ between the spin rotation plane and the normal direction of the layer [57].

Recent observations based on the optical second-harmonic generation technique revealed the presence of ferroelectric polarizations in ultrathin NiI$_2$ flake down to bilayer [48] and monolayer [49] limit below $T_{\mathrm{N},2} \simeq 20$ K, which suggested the survival of the 2D multiferroic and the helimagnetic order

---

[*] Contact author: kashen@bnu.edu.cn

therein. A sandwiched device with a trilayer $\mathrm{NiI_2}$ in between hexagonal boron nitride and graphene even showed room-temperature multiferroic, where the mutual control between magnetism and ferroelectricity was demonstrated [59]. Subsequently, the multiferroic order in monolayer $\mathrm{NiI_2}$ was directly probed through scanning tunneling microscopy [60] and spin-polarized scanning tunneling microscopy [61] at atomic scale, where the resulting spin modulation vector was found to differ from the bulk case, not only in its value but also in its direction [60]. Similar to the bulk case, a canting of the spin rotation plane was also observed in a monolayer $\mathrm{NiI_2}$ [61].

On the theoretical side, the existence of the multiferroic in $\mathrm{NiI_2}$ was supported by first-principles-based spin models in both bulk and 2D limit [50–53]. An isotropic Heisenberg model up to the third-nearest neighbors showed that the competition between exchange couplings is sufficient to establish a planar spin spiral along [110] direction in monolayer $\mathrm{NiI_2}$, with all spins orientated within the plane [52]. The inclusion of the spin-orbit coupling further resulted in a canting angle of the rotation plane $\sim 64^\circ$, which is comparable with the bulk value, with respect to the normal direction of the layer plane [52]. The density functional theory (DFT) calculations based on the Perdew-Burke-Ernzerhof (PBE) functional [62] with the spin-orbit coupling comprised self-consistently predicted a noncoplanar helix in monolayer $\mathrm{NiI_2}$ [53], which is, however, in conflict with the later observation of coplanar spin texture from spin-polarized scanning tunneling microscopy [61]. Alternatively, other calculations based on the HSE06 hybrid functional [63] and the PBE functional showed the presence of Kitaev and biquadratic interactions between the nearest neighbors, which are conducive to the coplanar spin spiral with a proper canting of the rotation plane in bulk $\mathrm{NiI_2}$ [50,51] as well as in monolayer limit [51]. However, as all possible choices of the spin spiral configurations in these works rely on the size of the supercells used in the calculation, whether the selected lowest-energy state is the ground state needs to be examined. Scanning tunneling microscopy actually revealed a slight deviation of the modulation vector from crystal axes [60], which cannot be well described by finite-supercell modeling. A self-consistent determination of the ground spin configuration in $\mathrm{NiI_2}$ thus remains to be developed. Furthermore, the spin excitation of the spin spiral in $\mathrm{NiI_2}$ is also far from clear.

In this work, we study the magnetic ground states with different interactions through an analytical method and confirm the formation of the helimagnetic structure. We find that, while the modulation vectors of the helimagnetic ground states from the isotropic models obey sixfold rotational symmetry including the [110] axis, the increase of the anisotropic Kitaev interaction gradually tilts the modulation vector toward $[1\bar{1}0]$ direction and causes a canting of the rotation plane in the helimagnetic structure. Then, we calculate the magnon spectra and the wave functions of magnons, which display anomalous behaviors around the center of the Brillouin zone (BZ). Specifically, we find soft magnons at finite wave vectors, which have zero frequency within the isotropic model, and gain a finite frequency from Kitaev interaction. The spin precession trajectories show that, in contrast to the normal Goldstone mode, which is polarized within the canting plane, such soft magnons correspond to linearly polarized dynamics normal to the canting plane. Finally, we investigate the thermal effects on the spectra of magnons and their transport and predict a magnetic phase transition driven by soft magnon as well as a sign change in the temperature dependence of the transverse thermal conductivity.

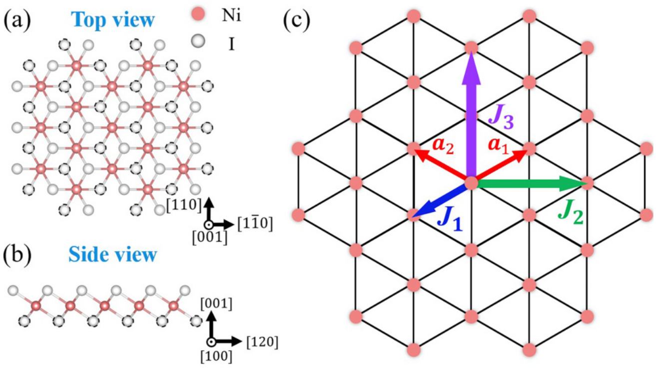

FIG. 1. (a) Top and (b) side views of a single-layer $\mathrm{NiI_2}$, where pink balls represent $\mathrm{Ni^{2+}}$ ions and the gray ones with (without) the black-dashed circles stand for the $\mathrm{I^-}$ ions below (above) the $\mathrm{Ni^{2+}}$ layer. (c) The simplified top view, where the nonmagnetic $\mathrm{I^-}$ are omitted. Two red arrows represent the basic translation vectors $\boldsymbol{a}_1$ and $\boldsymbol{a}_2$. Blue, green, and purple arrows indicate the nearest- (J_1), the next-nearest- (J_2), and the third-nearest-neighbor (J_3) exchange pairs.

II. MODEL AND FORMALISM

As schematically shown in Figs. 1(a) and 1(b), each $\mathrm{Ni^{2+}}$ ion is surrounded by six $\mathrm{I^-}$ ions. Those $\mathrm{I^-}$ ions with and without the black-dashed circles lie below and above the $\mathrm{Ni^{2+}}$ layer, respectively. The location of the $\mathrm{Ni^{2+}}$ indexed by (i, j) is described by $\boldsymbol{R}_{ij} = i\boldsymbol{a}_1 + j\boldsymbol{a}_2$ with $\boldsymbol{a}_1$ and $\boldsymbol{a}_2$ being the basic translation vectors as shown in Fig. 1(c). All magnetic moments come from $\mathrm{Ni^{2+}}$ with spin $S = 1$. The generalized spin exchange model with the Kitaev and biquadratic interactions is expressed by [50,51]

$$H = \sum_{\langle ij,i'j'\rangle_1} \{J_1 \boldsymbol{S}_{ij}\cdot\boldsymbol{S}_{i'j'} + K S^\gamma_{ij} S^\gamma_{i'j'} + B(\boldsymbol{S}_{ij}\cdot\boldsymbol{S}_{i'j'})^2\} + \sum_{\langle ij,i'j'\rangle_2} J_2 \boldsymbol{S}_{ij}\cdot\boldsymbol{S}_{i'j'} + \sum_{\langle ij,i'j'\rangle_3} J_3 \boldsymbol{S}_{ij}\cdot\boldsymbol{S}_{i'j'}, \tag{1}$$

where $\langle ij, i'j'\rangle_l$ denote the pairs of the lth-nearest neighbors and J_l correspond to the exchange constants as defined in Fig. 1(c). K and B are the strengths of the Kitaev and biquadratic interactions between the nearest neighbors. The Kitaev interaction describing the anisotropy of the exchange terms with $S^\gamma_{ij} = \boldsymbol{S}_{ij}\cdot\boldsymbol{\gamma}$, where $\boldsymbol{\gamma}$ is the Kitaev axis of a specific nearest-neighbor Ni-Ni bond [64], which is provided in Appendix A. Focusing on the spins of a single layer within the few-layer $\mathrm{NiI_2}$, we omit the interlayer exchange interactions following the previous work [50]. The single-ion anisotropy is also neglected because of its weak strength as found in both bulk [50] and monolayer [53] $\mathrm{NiI_2}$. Moreover, as a type-II multiferroic, the DM interaction does exist in $\mathrm{NiI_2}$, but it is also too weak to affect the spin texture and hence is neglected here.

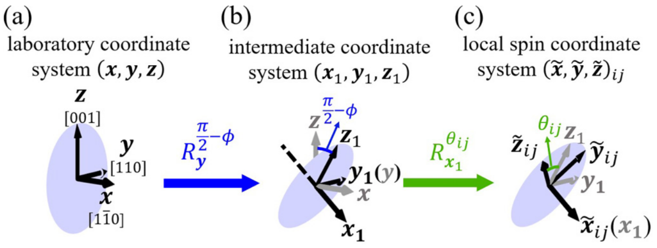

FIG. 2. Definition of the rotation transformations from the laboratory coordinate system (x, y, z) to the local spin coordinate system $(\tilde{x}, \tilde{y}, \tilde{z})_{ij}$, bridged by an intermediate system (x_1, y_1, z_1).

A. Representation in the local rotation frame

For a collinear magnetic ground state, it is common to project the spin Hamiltonian into the laboratory coordinate system, where one of the three axes is set to be along the magnetization direction. For a noncollinear spin configuration, however, a local spin coordinate system is more convenient for the study of spin excitation. Specified to the present case with a possible helimagnetic phase, we define the local spin coordinate system $(\tilde{x}, \tilde{y}, \tilde{z})_{ij}$ with $\tilde{z}_{ij}$ being the equilibrium direction of the spin at site (i, j).

By assuming the rotation plane of the helimagnetic configuration consistent with that in bulk, namely, with its normal vector in the (110) plane, which will be confirmed later by the positive definiteness condition of the magnon Hamiltonian, we define ϕ as the relative angle between the normal of the rotation plane and the [001] axis. Starting from the laboratory coordinate system (x, y, z) defined by the $[1\bar{1}0]$, [110], and [001] axes in Fig. 2(a), we introduce a global coordinate system (x_1, y_1, z_1) by rotating the laboratory coordinate one around the [110] axis by $(\pi/2) - \phi$ as shown by Fig. 2(b). The local spin coordinate system $(\tilde{x}, \tilde{y}, \tilde{z})_{ij}$ of each site then can be specified, as shown in Fig. 2(c), by further applying another rotation with θ_{ij}, which corresponds to the polar angle of the equilibrium spin with respect to the z_1 axis.

The transformation between the laboratory coordinate system and the local spin coordinate system is thus given by

$$S^{\alpha}_{ij} = \mathcal{R}^{\alpha\beta}_{ij}\tilde{S}^{\beta}_{ij}, \tag{2}$$

with the transformation matrix

$$\begin{aligned}\mathcal{R}_{ij} &= R^{\theta_{ij}}_{x_1} \times R^{\frac{\pi}{2}-\phi}_{y}\\ &= \begin{pmatrix} \sin\phi & \cos\phi\sin\theta_{ij} & \cos\phi\cos\theta_{ij}\\ 0 & \cos\theta_{ij} & -\sin\theta_{ij}\\ -\cos\phi & \sin\phi\sin\theta_{ij} & \sin\phi\cos\theta_{ij}\end{pmatrix},\end{aligned} \tag{3}$$

where $\theta_{ij} = \boldsymbol{q}\cdot\boldsymbol{R}_{ij}$ with $\boldsymbol{q}$ being the magnetic modulation vector of the helimagnetic structure.

Projecting Eq. (1) to $(\tilde{x}, \tilde{y}, \tilde{z})_{ij}$, the isotropic Heisenberg exchange terms and the biquadratic interaction lead to

$$H_{\text{iso}} = \sum_{l,\langle ij,i'j'\rangle_l} J_l\tilde{\mathcal{T}}_{ij,i'j'} + \sum_{\langle ij,i'j'\rangle_1} B(\tilde{\mathcal{T}}_{ij,i'j'})^2, \tag{4}$$

where the expression of $\tilde{\mathcal{T}}_{ij,i'j'}$ is

$$\begin{aligned}\tilde{\mathcal{T}}_{ij,i'j'} = {}& \tilde{S}^x_{ij}\tilde{S}^x_{i'j'} + \cos\Delta\theta_{i'j'}\tilde{S}^y_{ij}\tilde{S}^y_{i'j'} + \cos\Delta\theta_{i'j'}\tilde{S}^z_{ij}\tilde{S}^z_{i'j'}\\ & - \sin\Delta\theta_{i'j'}\tilde{S}^y_{ij}\tilde{S}^z_{i'j'} + \sin\Delta\theta_{i'j'}\tilde{S}^z_{ij}\tilde{S}^y_{i'j'},\end{aligned} \tag{5}$$

with $\Delta\theta_{i'j'} = \theta_{i'j'} - \theta_{ij}$. The anisotropic exchange due to the Kitaev interaction can be expressed by

$$H_{\text{ani}} = \sum_{\langle ij,i'j'\rangle_1} K\tilde{\mathcal{Y}}_{ij}\times\tilde{\mathcal{Y}}_{i'j'}. \tag{6}$$

The detailed expression of $\tilde{\mathcal{Y}}_{ij}$ is provided in Appendix A.

B. Ground-state energy

Since $\tilde{z}_{ij}$ is defined as the equilibrium orientation of the local spin, we substitute $\tilde{S}^z_{ij} = S$ and $\tilde{S}^x_{ij} = \tilde{S}^y_{ij} = 0$ into Eqs. (4) and (6) to calculate the ground-state energy of a helimagnetic configuration. The isotropic and the anisotropic exchange contributions separately give

$$E_{\text{iso}} = \sum_{l,\langle ij,i'j'\rangle_l} J_l S^2\cos\left(\boldsymbol{q}\cdot\boldsymbol{\delta}^{ij}_{i'j'}\right) + \sum_{\langle ij,i'j'\rangle_1} BS^4\cos^2\left(\boldsymbol{q}\cdot\boldsymbol{\delta}^{ij}_{i'j'}\right), \tag{7}$$

and

$$\begin{aligned}E_{\text{ani}} = {}& \sum_{ij} 2KS^2\cos^2(\boldsymbol{q}\cdot\boldsymbol{R}_{ij})\bigg\{\cos(q_y a)\xi_1^2(\phi)\\ & + \cos\left(\frac{\sqrt{3}q_x a}{2}\right)\cos\left(\frac{q_y a}{2}\right)\left[2\xi_2^2(\phi) - 1\right]\bigg\}\\ & + \sum_{ij} 2KS^2\cos\left(\frac{\sqrt{3}q_x a}{2}\right)\cos\left(\frac{q_y a}{2}\right).\end{aligned} \tag{8}$$

Here, $\boldsymbol{\delta}^{ij}_{i'j'} = \boldsymbol{R}_{i'j'} - \boldsymbol{R}_{ij}$, $\xi_1(\phi) = -\frac{\sqrt{2}}{\sqrt{3}}\cos\phi + \frac{1}{\sqrt{3}}\sin\phi$, and $\xi_2(\phi) = \frac{1}{\sqrt{6}}\cos\phi + \frac{1}{\sqrt{3}}\sin\phi$.

In order to derive the magnetic ground configuration, we need to find out $\boldsymbol{q}_{\text{G}}$ and ϕ_{G} for a minimum total energy $E_{\text{tot}} = E_{\text{iso}} + E_{\text{ani}}$. Since the canting angle ϕ is determined solely by the anisotropic energy due to the Kitaev interaction, we derive ϕ_{G} from the condition $\partial_\phi E_{\text{ani}}|_{\phi_{\text{G}}} = 0$ and $\partial^2_\phi E_{\text{ani}}|_{\phi_{\text{G}}} > 0$. After straightforward calculation, we obtain

$$\tan 2\phi_{\text{G}} = -2\sqrt{2}, \tag{9}$$

which corresponds to $\phi_{\text{G}} \approx 55^\circ$, consistent with the result from Ref. [50]. Substituting Eq. (9) into Eqs. (7) and (8), the total energy of the magnetic ground state is then expressed as

$$\begin{aligned}E_{\text{tot}} = {}& \sum_{l,\langle ij,i'j'\rangle_l} J_l S^2\cos\left(\boldsymbol{q}\cdot\boldsymbol{\delta}^{ij}_{i'j'}\right) + \sum_{\langle ij,i'j'\rangle_1} BS^4\cos^2\left(\boldsymbol{q}\cdot\boldsymbol{\delta}^{ij}_{i'j'}\right)\\ & + \sum_{ij} 2KS^2\cos\left(\frac{\sqrt{3}q_x a}{2}\right)\cos\left(\frac{q_y a}{2}\right).\end{aligned} \tag{10}$$

The possible ground-state configuration can be then obtained by further minimizing Eq. (10) with respect to $\boldsymbol{q}$, which can be achieved numerically as discussed later in Sec. III A. As mentioned above, the correctness of the ground state must be examined by the positive definiteness condition of the magnon Hamiltonian.

C. Magnon Hamiltonian

In order to derive the magnon Hamiltonian, we employ Holstein-Primakoff transformation [65] to the local spin operators in Eqs. (4) and (6) through

$$\begin{aligned}\tilde{S}^x_{ij} &\simeq \frac{\sqrt{2S}}{2}(\tilde{a}_{ij}+\tilde{a}^\dagger_{ij}),\\ \tilde{S}^y_{ij} &\simeq \frac{\sqrt{2S}}{2i}(\tilde{a}_{ij}-\tilde{a}^\dagger_{ij}),\\ \tilde{S}^z_{ij} &= S-\tilde{a}^\dagger_{ij}\tilde{a}_{ij},\end{aligned} \tag{11}$$

and perform Fourier transformation $\tilde{a}_{ij} = 1/\sqrt{N}\sum_{\boldsymbol{k}}\tilde{a}_{\boldsymbol{k}}e^{i\boldsymbol{k}\cdot\boldsymbol{R}_{ij}}$ to project the magnon operators into the momentum space. The resulting magnon Hamiltonian can be expressed as

$$\mathcal{H}_{\boldsymbol{k},-\boldsymbol{k}} = \mathcal{A}_{\boldsymbol{k}}(\tilde{a}^\dagger_{\boldsymbol{k}}\tilde{a}_{\boldsymbol{k}}+\tilde{a}^\dagger_{-\boldsymbol{k}}\tilde{a}_{-\boldsymbol{k}}) + \mathcal{B}_{\boldsymbol{k}}(\tilde{a}_{\boldsymbol{k}}\tilde{a}_{-\boldsymbol{k}}+\tilde{a}^\dagger_{\boldsymbol{k}}\tilde{a}^\dagger_{-\boldsymbol{k}}). \tag{12}$$

The detailed expressions of $\mathcal{A}_{\boldsymbol{k}}$ and $\mathcal{B}_{\boldsymbol{k}}$ can be found in Appendix B. The magnon Hamiltonian, i.e., Eq. (12), can be rewritten in the form of a matrix $H_{\boldsymbol{k}}$ under the basis of $(\tilde{a}_{\boldsymbol{k}}, \tilde{a}^\dagger_{-\boldsymbol{k}})$ as

$$\mathcal{H}_{\boldsymbol{k},-\boldsymbol{k}} = X^\dagger_{\boldsymbol{k},-\boldsymbol{k}}H_{\boldsymbol{k}}X_{\boldsymbol{k},-\boldsymbol{k}}, \tag{13}$$

where $X_{\boldsymbol{k},-\boldsymbol{k}} = [\tilde{a}_{\boldsymbol{k}} \quad \tilde{a}^\dagger_{-\boldsymbol{k}}]^T$ with $\tilde{a}_{\boldsymbol{k}}$ denoting the magnon annihilation operator for a wave vector $\boldsymbol{k}$. A true ground-state configuration requires that $H_{\boldsymbol{k}}$ must be positive definite, which corresponds to $|\mathcal{A}_{\boldsymbol{k}}|^2 - |\mathcal{B}_{\boldsymbol{k}}|^2 \geqslant 0$ in the present case.

In the case of a proper ground state, the magnon spectrum and the corresponding magnon wave functions can be obtained from the paraunitary diagonalization of $H_{\boldsymbol{k}}$ through

$$T^\dagger_{\boldsymbol{k},-\boldsymbol{k}}H_{\boldsymbol{k}}T_{\boldsymbol{k},-\boldsymbol{k}} = \begin{bmatrix}\hbar\omega_{\boldsymbol{k}} & 0\\ 0 & \hbar\omega_{-\boldsymbol{k}}\end{bmatrix}, \tag{14}$$

where $T_{\boldsymbol{k},-\boldsymbol{k}}$ is a paraunitary matrix derived from the Cholesky decomposition [66]. The magnon spectrum is then given by

$$\hbar\omega_{\boldsymbol{k}} = \sqrt{\mathcal{A}_{\boldsymbol{k}}{}^2 - \mathcal{B}_{\boldsymbol{k}}{}^2}, \tag{15}$$

and the corresponding operators of the magnon eigenmodes are

$$Z_{\boldsymbol{k},-\boldsymbol{k}} = [\tilde{\alpha}_{\boldsymbol{k}} \quad \tilde{\alpha}^\dagger_{-\boldsymbol{k}}]^T = T^{-1}_{\boldsymbol{k},-\boldsymbol{k}}X_{\boldsymbol{k},-\boldsymbol{k}}. \tag{16}$$

For a nonground state, $|\mathcal{A}_{\boldsymbol{k}}|^2 < |\mathcal{B}_{\boldsymbol{k}}|^2$ leads to an imaginary frequency in Eq. (15). For the sake of convenience, we will show the magnon excitation with an imaginary frequency by a negative frequency with the definition $-\hbar\omega_{\boldsymbol{k}} = -\sqrt{|\mathcal{A}_{\boldsymbol{k}}{}^2 - \mathcal{B}_{\boldsymbol{k}}{}^2|}$.

III. NUMERICAL RESULTS

For numerical calculations of the ground configuration and the magnon spectrum, we adopt parameters from previous first-principles study [50]. Specifically, we take the exchange parameters $J_1 = -4.976$ meV, $J_2 = 0.03J_1$, $B = 0.14J_1$, and $K = -0.17J_1$. Since the value of J_3 strongly relies on the functional used in the first-principles calculation [50,51], we treat the ratio of J_3/J_1 as an adjustable parameter with negative values by considering the antiferromagnetic nature of J_3 term [50,51].

A. Magnetic ground states

The magnetic ground state with the modulation of J_3 is carried out by searching the minimum of E_{tot} in Eq. (10) during the variation of $\boldsymbol{q}$ within the entire first BZ. In order to elucidate the role of different interactions, we perform calculations from three different models: (i) J_1-J_2-J_3 model with only isotropic Heisenberg exchange, (ii) J_1-J_2-J_3-B model with both Heisenberg and biquadratic interactions, and (iii) J_1-J_2-J_3-B-K with our full Hamiltonian in Eq. (1). The results of the ground states are summarized in Fig. 3.

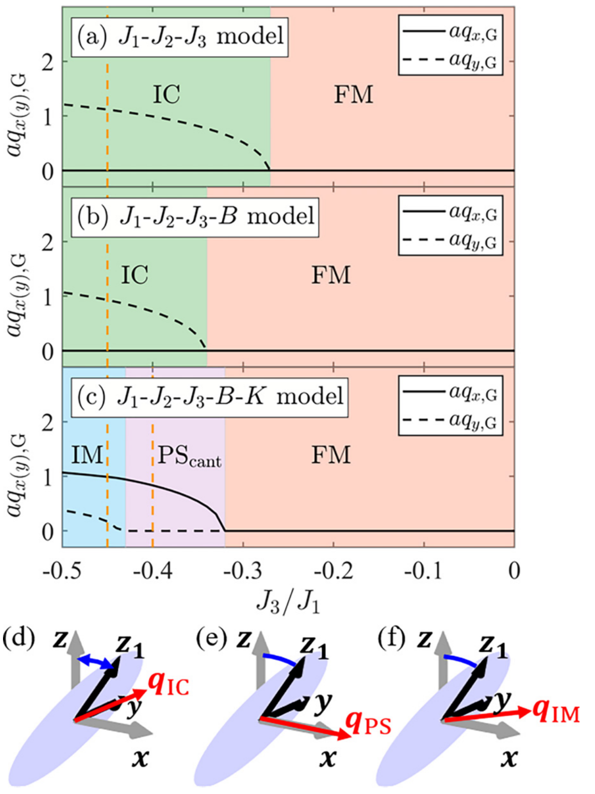

FIG. 3. Phase diagrams of the magnetic ground states with respect to the variation of $|J_3|$ from (a) J_1-J_2-J_3, (b) J_1-J_2-J_3-B, and (c) J_1-J_2-J_3-B-K models. The solid and dashed curves are the x and y components of the modulation vector $\boldsymbol{q}_{\mathrm{G}}$. (d)–(f) illustrate the spin rotation plane and the orientation of $\boldsymbol{q}_{\mathrm{G}}$ for IC, PS$_{\mathrm{cant}}$, and IM phases.

Figures 3(a) and 3(b) show that the ground state in J_1-J_2-J_3 and J_1-J_2-J_3-B models can be either a ferromagnetic (FM) phase (pink-shaded areas) or an incommensurate cycloid (IC) phase (green-shaded areas), resulting from the competition between the exchange terms. In a small J_3 limit, the ferromagnetic nearest-neighbor interaction makes all spins parallel with each other. As the magnitude of J_3 exceeds a critical value, an incommensurate cycloid along the y direction ([110] axis) is established, as illustrated in Fig. 3(d), with the value of the modulation vector q_{G} increasing with J_3. The absence of the Kitaev interaction makes the system isotropic and therefore the rotation plane of the IC phase can be of arbitrary values, according to Eq. (7). On the other hand, the sixfold rotational symmetry of the Ni^{2+} sublattice leads to the relation $E_{\mathrm{iso}}(0, \pm q_{\mathrm{G}}) = E_{\mathrm{iso}}(\pm\sqrt{3}q_{\mathrm{G}}/2, \pm q_{\mathrm{G}}/2)$, indicating six modulation vectors in total. The critical value of $|J_3|$ for the transition from the FM phase to the IC phase in J_1-J_2-J_3-B model is larger than the one in J_1-J_2-J_3 model, as the B term between the nearest neighbors effectively enhances the

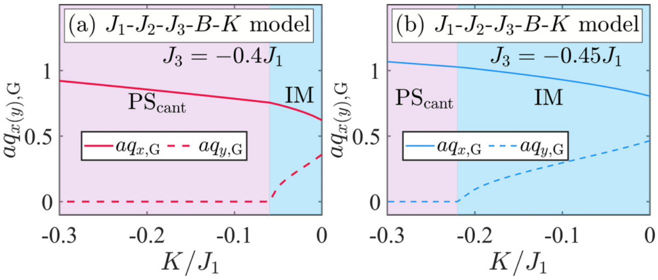

FIG. 4. Phase diagrams and the evolution of the modulation vectors by varying the Kitaev parameter in the J_1-J_2-J_3-B-K model with different values of J_3.

ferromagnetic coupling of J_1 and requires a larger J_3 to stabilize the cycloid configuration.

With the inclusion of the Kitaev interaction, the phase diagram of the magnetic ground states shown in Fig. 3(c) contains, in addition to the FM phase, a canted proper screw ($\mathrm{PS_{cant}}$) and an intermediate (IM) phase, which correspond to the modulation vector along x direction ([$1\bar{1}0$] axis) and in between x and y axes, respectively, as illustrated in Figs. 3(e) and 3(f). While the configuration of the $\mathrm{PS_{cant}}$ phase is consistent with the in-plane projection of bulk $\mathrm{NiI_2}$ [50], our finding of the IM phase nicely reproduces the recent observation from scanning tunneling microscopy measurement [60]. Note that, although our model and parameters are all the same as those in Ref. [50], our analytical calculation allows us to derive the precise ground state with any modulation vector, which is beyond the scope of the supercell calculation in Refs. [50,51,53]. For example, with $J_3 = -0.45J_1$, we obtain an IM ground state, while the rectangle supercell used in Ref. [50] leads to a modulation vector $\boldsymbol{q}_\mathrm{G}$ along [$1\bar{1}0$] or [110] direction with its magnitude matching the size of the supercell. Another noteworthy point is that the sixfold rotational symmetry of $\boldsymbol{q}_\mathrm{G}$ is broken in both $\mathrm{PS_{cant}}$ and IM phases, leaving only a reversal symmetry of $\pm\boldsymbol{q}_\mathrm{G}$. In addition, the Kitaev interaction aligns all spins within the canting plane even in the FM phase in Fig. 3(c).

As reported from the previous first-principles study, the Kitaev strength could be significantly reduced in a monolayer [51]. To show its consequence on the ground-state configuration, we plot the two components of the modulation vector as functions of the Kitaev strength in Fig. 4, which gives the transition from the $\mathrm{PS_{cant}}$ order to the IM state in the weak Kitaev region. The modulation vector $\boldsymbol{q}_\mathrm{G}$ of the IM state gradually rotates toward the [100] direction along the nearest Ni-Ni bond, which is equivalent to the y axis in the zero-K limit. Notice that for any finite K, the modulation vector deviates from the Ni-Ni bond, which explains the microscopy in monolayer $\mathrm{NiI_2}$ [60]. This feature, as explained above, cannot be captured by the supercell-based calculation commonly used for determining the ground-state spin configuration [50,51,53]. The reported helimagnetic ground states of $\mathrm{NiI_2}$ in the literatures are summarized in Table I in Appendix C.

B. Magnon spectra in helimagnetic phase

In this section, we discuss the property of the magnon spectra in the realistic helimagnetic ground states from different models discussed in the previous section. The main results are presented in Fig. 5, where the right panel of each subfigure is the enlarged view of the white parallelogram in the left plot. As seen, all of the spectra do not suffer from the imaginary-frequency problem, indicating that the helimagnetic phases for these calculations are indeed ground states, which also rules out the noncoplanar spin textures in the present case [53]. The first BZ is framed by the blue-dotted lines in Fig. 5(a) with the high-symmetry k points labeled. We can explicitly observe that the existence of a specific modulation vector breaks the six-fold rotational symmetry of the magnon spectra in all cases.

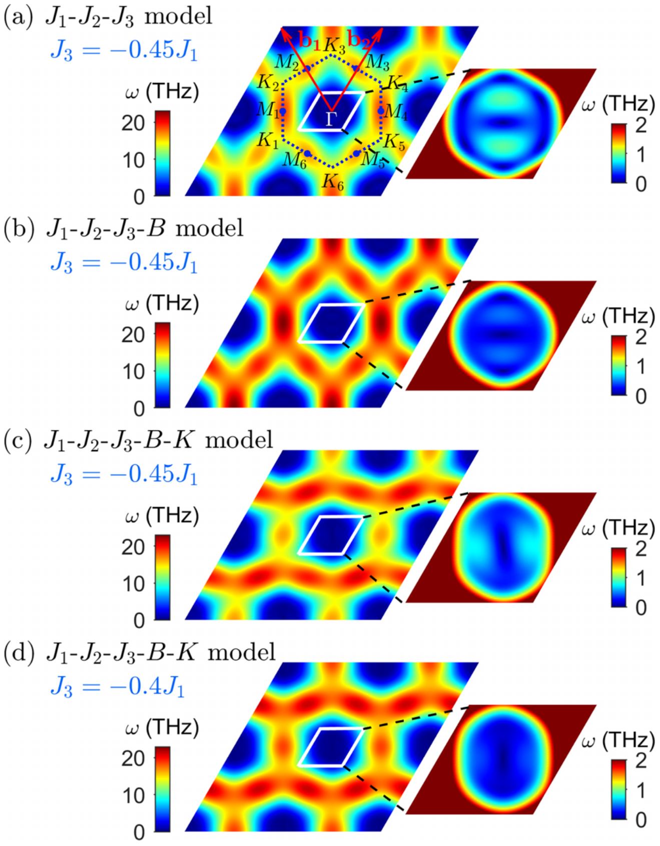

FIG. 5. The magnon spectra from different models. The red arrows in (a) are the reciprocal basis vectors and the blue-dotted lines frame the BZ with high-symmetry points indicated. The right panels in (a)–(d) are the enlarged views of the white-solid parallelograms in the main figures on the left.

By using the same models for Figs. 3(a) and 3(b), i.e., J_1-J_2-J_3 and J_1-J_2-J_3-B models, with $J_3 = -0.45J_1$, where the magnetic ground states are in the IC phase with $\boldsymbol{q}_\mathrm{G}$ along y axis indicated by the orange-dashed lines in Figs. 3(a) and 3(b), we obtain the magnon dispersions as shown in Figs. 5(a) and 5(b), respectively. These two spectra preserve the mirror symmetries with respect to the x and y axes. While the magnon frequencies at all K points are degenerate in these two cases, the frequencies at M_1 and M_4 are larger than those at the other M points. From the right panels, very interestingly, the dispersions around the BZ center exhibit complicated features with several local minima and local maxima, especially in y direction (along $\boldsymbol{q}_\mathrm{G}$).

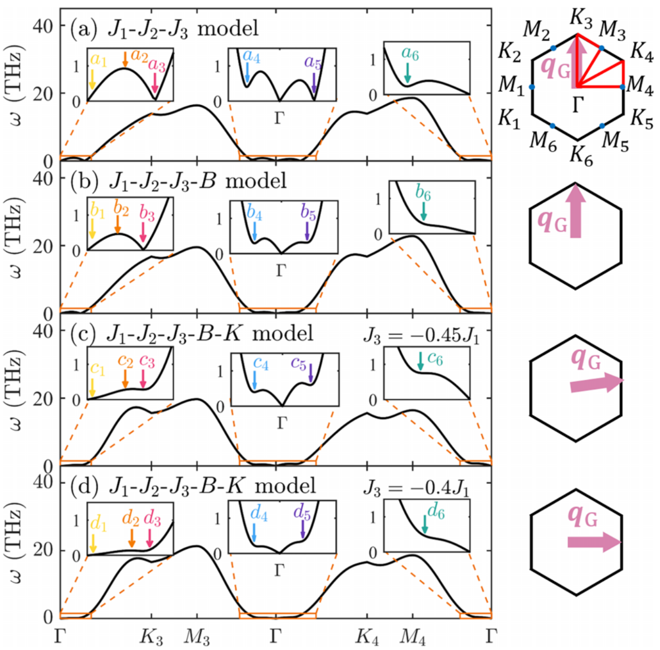

FIG. 6. The magnon dispersions along Γ-K_3-M_3-Γ-K_4-M_4-Γ path (left panel) and the illustrations of the corresponding modulation vectors (right panel). The insets are the enlarged views of the corresponding regions with the k points with anomalous features highlighted by colored arrows.

For the J_1-J_2-J_3-B-K model with Kitaev interaction, we choose two J_3 values, $J_3 = -0.45J_1$ and $J_3 = -0.4J_1$, whose magnetic ground states lie in the IM and $\mathrm{PS_{cant}}$ phases, respectively, indicated by the orange-dashed lines in Fig. 3(c). In the IM case, the mirror symmetries of the magnon spectrum with respect to the x and y axes are both broken as shown in Fig. 5(c), owing to the deviation of the $\boldsymbol{q}_\mathrm{G}$ from the x and y directions. For the $\mathrm{PS_{cant}}$ phase with $\boldsymbol{q}_\mathrm{G}$ along x direction in Fig. 5(d), the magnon spectrum satisfies the same mirror symmetries as those in the IC phase in Figs. 5(a) and 5(b). However, in contrast to Figs. 5(a) and 5(b), the magnon frequencies at M_1 and M_4 in Figs. 5(c) and 5(d) are smaller than those at the other M points. This feature and the distinct spectra around the BZ center reflect the consequence of the $\boldsymbol{q}_\mathrm{G}$ orientation.

To show the characteristic features around the BZ center more explicitly, we plot the dispersion curves along Γ-K_3-M_3-Γ-K_4-M_4-Γ path in Fig. 6. In the enlarged plots, we mark typical k points of anomalous dispersion with colored arrows. For comparison, magnon states in the normal linear-dispersion region are also taken as labeled by the a_1-d_1 with yellow arrows in the Γ-K_3 path. Specifically, in Fig. 6(a) from the J_1-J_2-J_3 model, zero-frequency states of finite wave vectors are observed at a_3 and a_5. These vectors coincide with two of the six equivalent modulation vectors of the IC phase, namely, $(0, q_\mathrm{G})$ and $(\sqrt{3}q_\mathrm{G}/2, q_\mathrm{G}/2)$, with which one can easily examine the relation $|\mathcal{A}| = |\mathcal{B}|$ in Eq. (15) by using the analytical expressions in Appendix B. The zero frequency of these modes reflects the global symmetry with respect to the continuous variation of ϕ for the spin rotation plane as discussed above. For the J_1-J_2-J_3-B model in Fig. 6(b), the biquadratic interaction leads to $|\mathcal{A}| \neq |\mathcal{B}|$ everywhere along the $(\sqrt{3}q/2, q/2)$ path, leaving only a local dip, instead of zero frequency, at b_5. In contrast, the zero-frequency mode remains available along the $(0, q)$ path at b_2, again reflecting the rotational symmetry of the IC ground state. When the Kitaev interaction is taken into account, all magnon frequencies at finite wave vectors become finite, as shown in Figs. 6(c) and 6(d), while the anomalous features can still be recognized at c_3 and c_5, as well as d_3 and d_5. The linear dispersion around the Γ point in all cases reflects the property of the Goldstone mode with all spins rotating simultaneously within the rotation plane, just like the situation in easy-plane magnets [67].

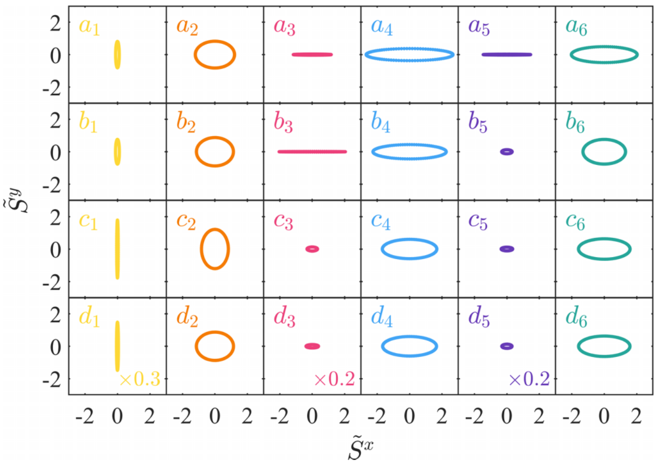

FIG. 7. The trajectories of spin precession in the local spin coordinate system at the k points marked in Fig. 6. The yellow, pink, and purple trajectories are multiplied by factors indicated in the figures for plotting.

The dynamic properties of the magnon modes around the anomalous dispersion points in Fig. 6 are then analyzed from their wave functions. According to Eq. (16), the eigenstates of magnons can be written as

$$\tilde{\alpha}_{\boldsymbol{k}} = \left(T^{-1}_{\boldsymbol{k},-\boldsymbol{k}}\right)_{11}\tilde{a}_{\boldsymbol{k}} + \left(T^{-1}_{\boldsymbol{k},-\boldsymbol{k}}\right)_{12}\tilde{a}^{\dagger}_{-\boldsymbol{k}}. \tag{17}$$

By substituting the $\tilde{a}_{\boldsymbol{k}} = \tilde{S}^x_{\boldsymbol{k}} - i\tilde{S}^y_{\boldsymbol{k}}$, the dynamical components of the magnetization in the local spin coordinate system can be expressed as [68]

$$\begin{aligned}\tilde{S}^x_{\boldsymbol{k}}(t) &= \Re\left\{\left[\left(T^{-1}_{\boldsymbol{k},-\boldsymbol{k}}\right)_{11} + \left(T^{-1}_{\boldsymbol{k},-\boldsymbol{k}}\right)_{12}\right]e^{-i\omega_{\boldsymbol{k}}t}\right\},\\ \tilde{S}^y_{\boldsymbol{k}}(t) &= \Im\left\{\left[\left(T^{-1}_{\boldsymbol{k},-\boldsymbol{k}}\right)_{11} - \left(T^{-1}_{\boldsymbol{k},-\boldsymbol{k}}\right)_{12}\right]e^{-i\omega_{\boldsymbol{k}}t}\right\}.\end{aligned} \tag{18}$$

The spin precession trajectories at the k points labeled in Fig. 6 are plotted in Fig. 7. It is clear to find out that the zero-frequency modes at a_3, a_5, and b_3 all present linear vibration out of the rotation plane, i.e., the $\tilde{y}$-$\tilde{z}$ plane, corresponding to the variation of ϕ, as illustrated in Fig. 8(a). We should point out that the magnitude of dynamical components is arbitrarily large for the exact zero-frequency mode, therefore, we here use the wave vectors slightly away from these points for their plots. For those low-frequency magnons near the Γ point, the spin trajectory also presents a similar linearlike feature, as shown by the yellow curves in Fig. 7, especially for c_1 and d_1 with lower frequencies. The polarization direction of a_1-d_1 is along $\tilde{y}$ direction within the rotation plane [see Fig. 8(b)],

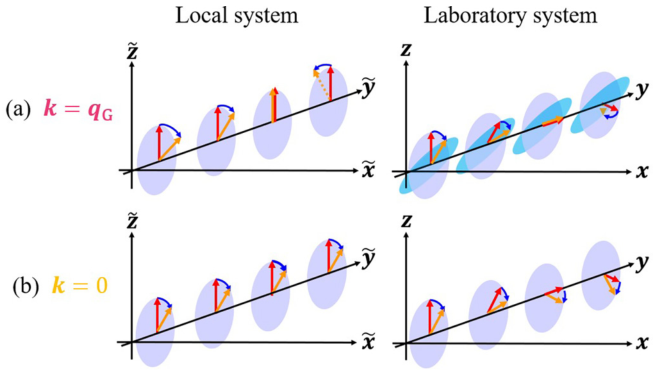

FIG. 8. Illustrations of the soft magnon modes at $\boldsymbol{k} = \boldsymbol{q}_{\mathrm{G}}$ and $\boldsymbol{k} = 0$ in the local and laboratory coordinate systems.

defined by the symmetry of the models [67], which is perpendicular to that of a_3, a_5, and b_3 along $\tilde{x}$ direction. Further, from the evolution of trajectories from a_3 to d_3 and from a_5 to d_5, we find that a finite frequency of the soft magnon, introduced by different parameters, generally changes the linear polarization to the elliptical polarization. When the frequency approaches the local maximum at a_2 or b_2, the precession can become nearly a circular shape.

C. Thermal effects

In this section, we investigate the thermal effects in the magnon spectra due to the enhanced magnon-magnon interaction as the temperature increases. In the two-dimensional limit, the gapless magnon dispersion causes an infrared divergence at finite temperature, according to the Mermin-Wagner theorem [69]. The direct calculation of the expectation value of the spin excitation $\overline{\Delta S} = \langle \tilde{a}_{\boldsymbol{k}}^{\dagger} \tilde{a}_{\boldsymbol{k}} \rangle$ in the present case does lead to a $\ln k$ divergence [68,70,71]. This suggests the destruction of the long-range magnetic order in two-dimensional limit by thermal effects. However, the previous experiments did observe the magnetic order at finite temperature [49,60,61], which might imply the influence of substrate by opening a finite magnon gap through some additional interactions. While the specific reasons for the survival of magnetic order down to monolayer NiI$_2$ at finite temperature need further experimental and theoretical studies, here, we analyze the thermal effects qualitatively by considering the effective spin $\langle S \rangle$ with its reduction due to the thermally excited magnon populations taken into account [68,70]. The finite-temperature magnon spectra then can be calculated from the mean-field technique by replacing the spin magnitude S in Sec. II B and Sec. II C by $\langle S \rangle$. Although a further self-consistent calculation is doable in principle [68], here, we stop at this first-order approximation due to the complicity of the present spin configuration, which is fortunately sufficient to capture qualitatively the consequence of thermal magnon excitation.

In this calculation, we use J_1-J_2-J_3-B-K model with $J_3 = -0.4J_1$ The magnon dispersion curves are plotted along Γ-K_3-M_3-Γ-K_4-M_4-Γ path in Fig. 9(a) for different values of $\langle S \rangle$. It can be explicitly seen that the biquadratic term, which is a fourth-order interaction of spin, competes with the other interactions in the second order and leads to the change of the magnon spectrum beyond a simple rescaling with $\langle S \rangle$.

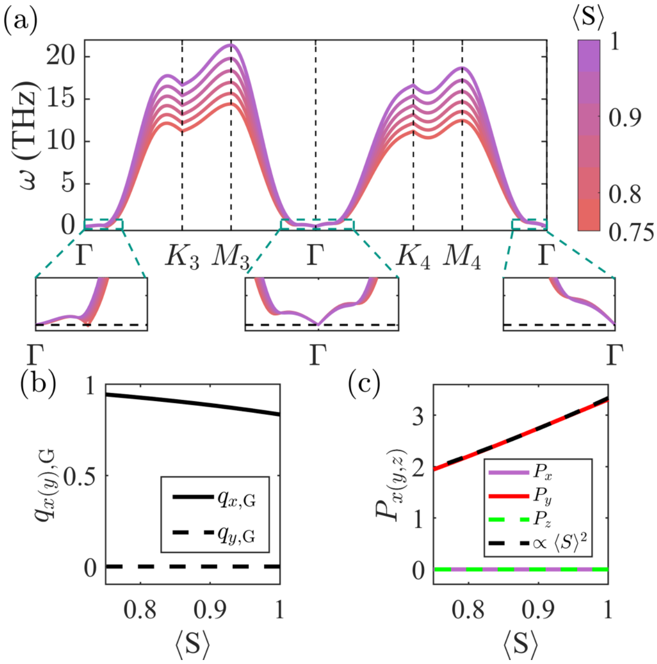

FIG. 9. (a) The magnon dispersions at finite temperatures, where the black-dashed lines in the enlarged views label the frequency $\omega = 0$. (b) The modulation vector and (c) the ferroelectric polarization as functions of the effective spin $\langle S \rangle$ derived from the helimagnetic structure.

The evolution of the helimagnetic state from the minimization procedure of E_{tot} in Eq. (10) is also shown in Fig. 9(b), which indicates that the spin configuration remains a PS$_{\mathrm{scant}}$ state with the spiral period decreasing at small $\langle S \rangle$. The left enlarged view of magnon spectra in Fig. 9(a), however, shows that the frequency of the soft magnon becomes imaginary at $\langle S \rangle = 0.75$. This means that the presumed helimagnetic configuration is not the equilibrium state any longer, suggesting a magnetic phase transition.

As the precise prediction of the ground state after the phase transition is rather challenging, the spatial modulation of the canting angle is found to be a possible reason for the transition. As shown in Fig. 10, in the present PS$_{\mathrm{cant}}$ structure with the modulation vector along the x direction, the spins located along the y axis all point to the same direction. A finite wave vector in Γ-K_3 path (in y direction) leads to these spins out of the canting plane with spatially modulated magnitudes, corresponding to a y-dependent variation of the canting angle

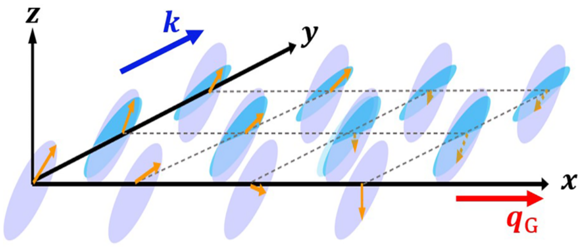

FIG. 10. Illustration of the magnetic phase transition driven by the spatial modulation of the canting plane.

ϕ. The imaginary frequency of this magnon mode means that such a modulation actually reduces the total energy and drives the system to leave the presumed helimagnetic configuration with a global constant ϕ permanently, causing the magnetic phase transition. This magnetic phase transition is under-reported, which might be ascribed to the incomplete studies, especially in few-layer NiI$_2$, or the absence of this new phase in those systems under study, possibly, due to the improper material parameters there [51,60,61]. If the issue of parameters occurs, then it might be possible to use different substrates to tune the parameters in few-layer NiI$_2$ and examine the presence of the magnetic transition through, for instance, the measurement of the magnetic susceptibility.

As mentioned before, NiI$_2$ is a type-II multiferroic material, whose ferroelectric polarization is induced by the spiral spin order through inverse DM mechanism. The variation of the spin spiral modulation in Fig. 9(b) also leads to a change in the ferroelectric polarization. We calculate the induced electric polarization from

$$\boldsymbol{P} \propto \sum_{\langle ij,i'j'\rangle_1} \boldsymbol{\delta}_{ij}^{i'j'} \times (\boldsymbol{S}_{ij} \times \boldsymbol{S}_{i'j'}). \tag{19}$$

As shown in Fig. 9(c), the resulting ferroelectric order only has a P_y component because the modulation vectors are along x direction. As the effective spin $\langle S\rangle$ decreases, P_y follows nicely with $\langle S\rangle^2$ (see the black dashed curve), where the reduction of $\langle S\rangle$ dominates the enhancement of the polarization due to the increase of modulation vector in Fig. 9(c). The suppression of electric polarization by thermal effect is also consistent with experimental observations [54].

D. Thermal conductivity

The strong anisotropy of the low-frequency magnon spectra shown in Fig. 5 is expected to give anisotropic thermal transport in the presence of a temperature gradient. In the linear response formalism, the heat current due to magnon transport can be expressed as

$$\boldsymbol{j} = -\boldsymbol{\kappa} \cdot \nabla T, \tag{20}$$

where the components of thermal conductivity matrix read [72]

$$\kappa_{\gamma\zeta} = \frac{1}{k_{\mathrm{B}}T^2} \int \frac{d^2\boldsymbol{k}}{(2\pi)^2} \tau_{\boldsymbol{k}} (\partial_{k_\gamma}\omega_{\boldsymbol{k}})(\partial_{k_\zeta}\omega_{\boldsymbol{k}}) \frac{e^{\beta\hbar\omega_{\boldsymbol{k}}}(\hbar\omega_{\boldsymbol{k}})^2}{(e^{\beta\hbar\omega_{\boldsymbol{k}}}-1)^2}, \tag{21}$$

with $\beta = 1/(k_{\mathrm{B}}T)$ and $\gamma, \zeta \in \{x, y\}$. Here, $\tau_{\boldsymbol{k}}^{-1}$ is the scattering rate of magnons, which could be quantitatively calculated by considering magnon-phonon interaction [72,73] or magnon-magnon interaction [74,75], and so on. For the present calculation, we treat it as a constant with $\tau = 1$ ns by assuming its weak dependence on the temperature in the region we considered (below 30 K).

The calculated longitudinal and transverse thermal conductivities based on J_1-J_2-J_3-B-K model with $J_3 = -0.4J_1$ are depicted in Fig. 11(a) as functions of temperature. One can see the transverse heat conductivity $\kappa_{xy} = 0$, because of the mirror symmetries with respect to the x and y axes. For the longitudinal components, κ_{xx} is considerably larger than κ_{yy} below 5 K as expected by the relation $v_x > v_y$ of the low-frequency magnons, which can be observed from the enlarged view of the Fig. 5(d) and the slope of the dispersion in Fig. 6.

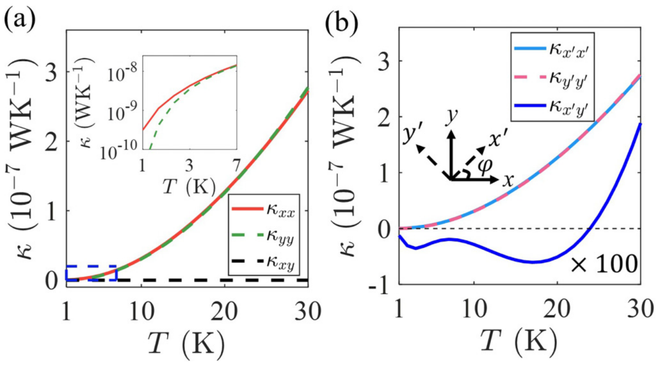

FIG. 11. (a) The temperature dependence of longitudinal thermal conductivities $\kappa_{xx(yy)}$ and transverse thermal conductivities κ_{xy}. (b) The temperature dependence of the rotated thermal conductivities with a rotation angle at $\varphi = 30^\circ$.

To describe the magnon heat current with a temperature gradient in an arbitrary direction, we project the thermal conductivity tensor into a rotated frame (x', y', z') through the transformation

$$\kappa_{m'n'} = \sum_{m,n} R_{m'm} R_{n'n} \kappa_{mn}, \tag{22}$$

where R corresponds to the transformation matrix between coordinate systems

$$\begin{pmatrix} x' \\ y' \\ z' \end{pmatrix} = \begin{pmatrix} \cos\varphi & \sin\varphi & 0 \\ -\sin\varphi & \cos\varphi & 0 \\ 0 & 0 & 1 \end{pmatrix} \begin{pmatrix} x \\ y \\ z \end{pmatrix}. \tag{23}$$

This will lead to a transverse thermal conductivity

$$\kappa_{x'y'} = \sin\varphi\cos\varphi(\kappa_{yy} - \kappa_{xx}), \tag{24}$$

of which the sign is determined by the relative values of κ_{yy} and κ_{xx} for a given φ. The numerical results with $\varphi = 30^\circ$ are presented in Fig. 11(b), where a sign change is observed for $\kappa_{x'y'}$ around 23 K. Above $T > 23$ K, the large population of the high-frequency magnons, which satisfies $v_y > v_x$, dominates the thermal transport and makes $\kappa_{yy} > \kappa_{xx}$. In addition to the sign change, the value of $\kappa_{x'y'}$ also shows a nonmonotonic temperature dependence below 23 K, due to the complicated features of the low-frequency spectrum.

IV. DISCUSSION

In Sec. III B, we focus on the magnon spectra in the helimagnetic phases. By calculating their magnon spectra with the formalism in Appendix B, we confirm that the FM states shown in Fig. 3 are indeed ground states in the corresponding weak J_3 region. The dispersion curves along Γ-K_3-M_3-Γ-K_4-M_4-Γ path from different models with $J_3 = -0.2J_1$ are shown in Figs. 12(a)–12(c). It could be explicitly seen that the magnon dispersions near Γ points become parabolic and the frequencies at all M points become degenerate, recovering the sixfold rotational symmetry in the entire BZ.

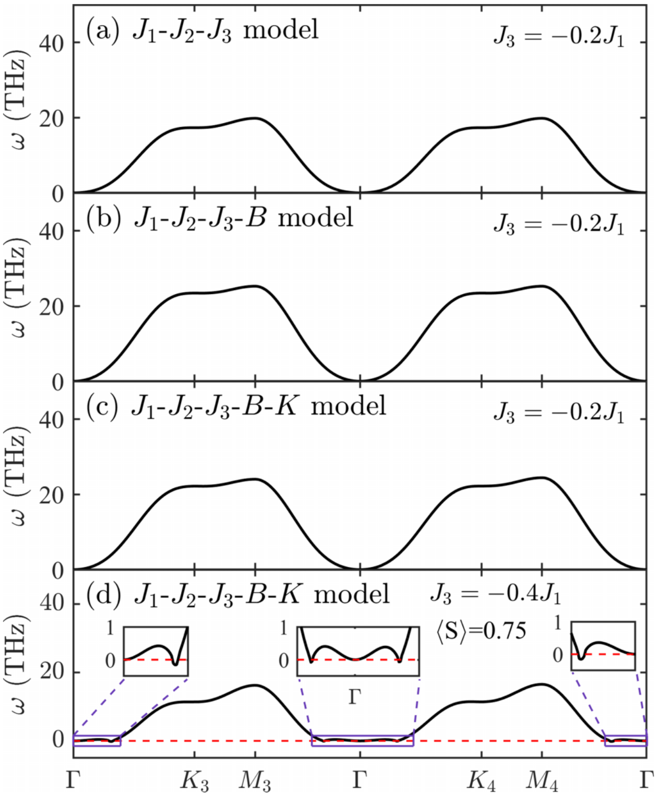

FIG. 12. The magnon dispersions along Γ-K_3-M_3-Γ-K_4-M_4-Γ path in the FM phase of different models at (a)–(c) $\langle S\rangle = 1$ and (d) $\langle S\rangle = 0.75$. The insets in (d) are the enlarged views of the low-frequency regions.

In Sec. III C, we predict the breakdown of the helimagnetic structure when $\langle S\rangle \leqslant 0.75$. In a recent work [76], the weak ferromagnetism was found to survive up to the room temperature in a NiI_2 flake with a thickness ∼10 μm. It is thus necessary to check if the FM states would be the thermal equilibrium states after the phase transition in our two-dimensional model. Therefore, we calculate the magnon spectrum from J_1-J_2-J_3-B-K model in the FM phase with $J_3 = -0.4J_1$ at $\langle S\rangle = 0.75$. The magnon dispersions plotted in Fig. 12(d) still show imaginary frequencies, indicating that the FM state cannot be the thermal equilibrium state or even a metastable state after the phase transition. In the bulk case, the antiferromagnetic phase with intralayer ferromagnetic order in the temperature region between $T_{N,1}$ and $T_{N,2}$ might imply the relevance of the interlayer coupling.

V. CONCLUSION

In summary, we adopted a realistic spin model containing isotropic exchange, biquadratic and Kitaev interactions to investigate the spin configurations of magnetic ground states in the vdW NiI_2, where a FM phase and three helimagnetic phases, i.e., IC, PS_{cant}, and IM phases, were discovered with different parameters. When only the isotropic terms, i.e., the Heisenberg exchange and biquadratic interactions, are considered, the magnetic ground states can be either a FM phase or an IC one. The modulation vector of the IC phase is along the [110] axis or its five equivalents under a sixfold rotation symmetry. Such a sixfold symmetry is broken when the Kitaev interaction is included, where the magnetic ground state changes from the FM phase to two helimagnetic phases with increasing the value of antiferromagnetic coupling between the third-nearest neighbors for a given strength of Kitaev interaction, namely, the PS_{cant} phase with the modulation vector along $[1\bar{1}0]$ axis and the IM phase with the modulation vector lying between [100] and $[1\bar{1}0]$ axes. The transition between PS_{cant} and IM phases was also found to be achievable by tuning the Kitaev strength. In addition, while the spin rotation plane of the helimagnetic structure is arbitrary in the isotropic model, the Kitaev interaction leads to a well-defined canting angle of the rotation plane for all FM, PS_{cant}, and IM phases.

The thermal stabilities of the obtained magnetic structures were then verified through the absence of imaginary frequencies in the magnon spectra. The magnon dispersion in the FM phase obeys a sixfold rotational symmetry with a standard parabolic dispersion in the long-wavelength region. In the helimagnetic phases, however, we found that the established spiral breaks the sixfold rotational symmetry of the magnon spectra but retains the mirror symmetries with respect to the x and y directions for IC and PS_{cant} phase. For the IM phase, these mirror symmetries are also violated. From an explicit analysis of the magnon spectra, in addition to the linear dispersion of the Goldstone mode in the long-wavelength region, we also found anomalous reductions of the frequency at finite wave vectors, which was recognized as soft magnons with linear polarization normal to the equilibrium spin rotation plane. Contrarily, the spin dynamics of the Goldstone mode show a linear polarization within the rotation plane and those magnon states with high frequencies give nearly a circular precession.

Moreover, we studied the thermal effects on the magnon spectra of the PS_{cant} phase based on a mean-field approach, where we predicted the breakdown of the helimagnetic structure when effective spin $\langle S\rangle \leqslant 0.75$ by recognizing the occurrence of the imaginary frequencies of the soft modes. This implies a magnetic phase transition driven by the soft magnons, which causes an instability in the global canting plane and tends to generate a spatial modulation to the canting angle. Before the phase transition, the period of the helimagnetic structure was found to be compressed by the reduction of the effective spin due to the thermal magnon population, which also suppresses the induced ferroelectric polarization via inverse DM mechanism. Finally, we calculated the thermal conductivities and found a sign change in the temperature dependence of the transverse thermal conductivity.

From the perspective of application, the local minima of magnon energies at soft magnon modes could host the magnon Bose-Einstein condensation [77–79] and might give negative differential thermal conductivity, which is similar to the negative differential conductivity in charge transport [80,81]. On the other hand, the ferroelectric polarization in NiI_2 originates from the spin texture, whose modification associated with soft magnons can also affect the magnitude of the induced ferroelectric polarization. The sign change of the transverse thermal conductivity or the thermal Hall conductivity is considered to be a unique probe of nontrivial topological excitations and the topological phase transition [82,83]. Our results reveal a similar sign reversal from an alternative mechanism, i.e., the strong frequency-dependent anisotropy of the magnon spectrum, which might be helpful in analyzing the origins of this phenomenon in real materials with/without topological excitations.

ACKNOWLEDGMENTS

This work was supported by the National Key R&D Program of China (Grant No. 2021YFA0718700), the National Natural Science Foundation of China (Grants No. 11974047 and No. 12374100) and the Fundamental Research Funds for the Central Universities. We thank Xuanyi Li at Fudan University for valuable discussions.

APPENDIX A: DETAILS OF KITAEV INTERACTION

The Kitaev interaction depends on the direction of Ni-Ni bond with $S^\gamma = \boldsymbol{S}\cdot\boldsymbol{\gamma}$ and $\boldsymbol{\gamma} = \boldsymbol{\alpha}\times\boldsymbol{\beta}$, where $\boldsymbol{\alpha}$ points from Ni_{ij} to its nearest neighbor $\mathrm{Ni}_{i'j'}$ and $\boldsymbol{\beta}$ is in the direction of two I ligands connecting Ni_{ij}-$\mathrm{Ni}_{i'j'}$ pair [84]. Using the atomic positions of different Ni-I bonds, the explicit expressions of $\boldsymbol{\gamma}$ axes are derived as

$$\begin{aligned}
\boldsymbol{\gamma}_{i-1,j-1} &= \boldsymbol{\gamma}_{i+1,j+1} = \left(-\frac{\sqrt{2}}{\sqrt{3}}, 0, \frac{1}{\sqrt{3}}\right),\\
\boldsymbol{\gamma}_{i,j-1} &= \boldsymbol{\gamma}_{i,j+1} = \left(\frac{1}{\sqrt{6}}, \frac{1}{\sqrt{2}}, \frac{1}{\sqrt{3}}\right),\\
\boldsymbol{\gamma}_{i-1,j} &= \boldsymbol{\gamma}_{i+1,j} = \left(\frac{1}{\sqrt{6}}, -\frac{1}{\sqrt{2}}, \frac{1}{\sqrt{3}}\right).
\end{aligned} \tag{A1}$$

In the main text, the contributions from Kitaev interaction can be written as Eq. (6), where $\tilde{\mathcal{Y}}_{ij}$ is expressed as

$$\tilde{\mathcal{Y}}_{ij} = \mathcal{O}_{ij}^{\boldsymbol{\gamma}_{i'j'}}\tilde{S}_{ij}^x + \mathcal{P}_{ij}^{\boldsymbol{\gamma}_{i'j'}}\tilde{S}_{ij}^y + \mathcal{Q}_{ij}^{\boldsymbol{\gamma}_{i'j'}}\tilde{S}_{ij}^z. \tag{A2}$$

For the Kitaev axes between $(i+1, j+1)$ and $(i-1, j-1)$ neighbors, the parameters are

$$\begin{aligned}
\mathcal{O}_{ij}^{\boldsymbol{\gamma}_{i+1,j+1(i-1,j-1)}} &= \zeta_1(\phi),\\
\mathcal{P}_{ij}^{\boldsymbol{\gamma}_{i+1,j+1(i-1,j-1)}} &= \xi_1(\phi)\sin\theta_{ij},\\
\mathcal{Q}_{ij}^{\boldsymbol{\gamma}_{i+1,j+1(i-1,j-1)}} &= \xi_1(\phi)\cos\theta_{ij},
\end{aligned} \tag{A3}$$

with $\zeta_1(\phi) = -\frac{\sqrt{2}}{\sqrt{3}}\sin\phi - \frac{1}{\sqrt{3}}\cos\phi$ and $\xi_1(\phi) = -\frac{\sqrt{2}}{\sqrt{3}}\cos\phi + \frac{1}{\sqrt{3}}\sin\phi$. The substitution of the Kitaev axes between $(i+1, j)$ and $(i-1, j)$ neighbors gives

$$\begin{aligned}
\mathcal{O}_{ij}^{\boldsymbol{\gamma}_{i+1,j(i-1,j)}} &= \zeta_2(\phi),\\
\mathcal{P}_{ij}^{\boldsymbol{\gamma}_{i+1,j(i-1,j)}} &= \xi_2(\phi)\sin\theta_{ij} - \frac{1}{\sqrt{2}}\cos\theta_{ij},\\
\mathcal{Q}_{ij}^{\boldsymbol{\gamma}_{i+1,j(i-1,j)}} &= \xi_2(\phi)\cos\theta_{ij} + \frac{1}{\sqrt{2}}\sin\theta_{ij},
\end{aligned} \tag{A4}$$

with $\zeta_2(\phi) = \frac{1}{\sqrt{6}}\sin\phi - \frac{1}{\sqrt{3}}\cos\phi$ and $\xi_2(\phi) = \frac{1}{\sqrt{6}}\cos\phi + \frac{1}{\sqrt{3}}\sin\phi$. For the Kitaev axes between $(i, j+1)$ and $(i, j-1)$ neighbors, we have

$$\begin{aligned}
\mathcal{O}_{ij}^{\boldsymbol{\gamma}_{i,j+1(i,j-1)}} &= \zeta_2(\phi),\\
\mathcal{P}_{ij}^{\boldsymbol{\gamma}_{i,j+1(i,j-1)}} &= \xi_2(\phi)\sin\theta_{ij} + \frac{1}{\sqrt{2}}\cos\theta_{ij},\\
\mathcal{Q}_{ij}^{\boldsymbol{\gamma}_{i,j+1(i,j-1)}} &= \xi_2(\phi)\cos\theta_{ij} - \frac{1}{\sqrt{2}}\sin\theta_{ij}.
\end{aligned} \tag{A5}$$

APPENDIX B: DETAILED EXPRESSIONS OF MAGNON HAMILTONIAN

In this Appendix, we provide the detailed expressions of the coefficients in the magnon Hamiltonian in Sec. II B. Specifically, we define

$$\frac{\mathcal{A}_{\boldsymbol{k}}}{S} = \mathcal{C}_{\boldsymbol{k}} + \mathcal{F}_{\boldsymbol{k}} + \mathcal{I}_{\boldsymbol{k}}, \tag{B1}$$

$$\frac{\mathcal{B}_{\boldsymbol{k}}}{S} = \mathcal{D}_{\boldsymbol{k}} + \mathcal{G}_{\boldsymbol{k}} + \mathcal{J}_{\boldsymbol{k}}, \tag{B2}$$

where $\mathcal{C}_{\boldsymbol{k}}$, $\mathcal{F}_{\boldsymbol{k}}$, $\mathcal{I}_{\boldsymbol{k}}$, $\mathcal{D}_{\boldsymbol{k}}$, $\mathcal{G}_{\boldsymbol{k}}$, and $\mathcal{J}_{\boldsymbol{k}}$ are expressed as

$$\begin{aligned}
\mathcal{C}_{\boldsymbol{k}} = \sum_{l,\langle ij,i'j'\rangle_l} J_l\big\{&\cos\big(\boldsymbol{k}\cdot\boldsymbol{\delta}_{i'j'}^{ij}\big)\big[1+\cos\big(\boldsymbol{q}\cdot\boldsymbol{\delta}_{i'j'}^{ij}\big)\big]\\
&-2\cos\big(\boldsymbol{q}\cdot\boldsymbol{\delta}_{i'j'}^{ij}\big)\big\},
\end{aligned} \tag{B3}$$

$$\begin{aligned}
\mathcal{F}_{\boldsymbol{k}} = 2BS^2\sum_{\langle ij,i'j'\rangle_1}\big\{&\cos\big(\boldsymbol{q}\cdot\boldsymbol{\delta}_{i'j'}^{ij}\big)\cos\big(\boldsymbol{k}\cdot\boldsymbol{\delta}_{i'j'}^{ij}\big)\\
&+\cos\big(2\boldsymbol{q}\cdot\boldsymbol{\delta}_{i'j'}^{ij}\big)\big[\cos\big(\boldsymbol{k}\cdot\boldsymbol{\delta}_{i'j'}^{ij}\big)-2\big]\\
&-\sin^2\big(\boldsymbol{q}\cdot\boldsymbol{\delta}_{i'j'}^{ij}\big)\big\},
\end{aligned} \tag{B4}$$

$$\begin{aligned}
\mathcal{I}_{\boldsymbol{k}} = K\big\{&\cos\big(\boldsymbol{q}\cdot\boldsymbol{\delta}_{i+1,j}^{ij}\big)\big[\cos\big(\boldsymbol{k}\cdot\boldsymbol{\delta}_{i+1,j}^{ij}\big)-2\big]\\
&+\cos\big(\boldsymbol{q}\cdot\boldsymbol{\delta}_{i,j+1}^{ij}\big)\big[\cos\big(\boldsymbol{k}\cdot\boldsymbol{\delta}_{i,j+1}^{ij}\big)-2\big]\\
&+2\cos\big(\boldsymbol{k}\cdot\boldsymbol{\delta}_{i+1,j+1}^{ij}\big)\big\}.
\end{aligned} \tag{B5}$$

$$\mathcal{D}_{\boldsymbol{k}} = \sum_{l,\langle ij,i'j'\rangle_l} J_l\cos\big(\boldsymbol{k}\cdot\boldsymbol{\delta}_{i'j'}^{ij}\big)\big[1-\cos\big(\boldsymbol{q}\cdot\boldsymbol{\delta}_{i'j'}^{ij}\big)\big], \tag{B6}$$

$$\begin{aligned}
\mathcal{G}_{\boldsymbol{k}} = 2BS^2\sum_{\langle ij,i'j'\rangle_1}&\big\{\cos\big(\boldsymbol{q}\cdot\boldsymbol{\delta}_{i'j'}^{ij}\big)\cos\big(\boldsymbol{k}\cdot\boldsymbol{\delta}_{i'j'}^{ij}\big)\\
&-\cos\big(2\boldsymbol{q}\cdot\boldsymbol{\delta}_{i'j'}^{ij}\big)\cos\big(\boldsymbol{k}\cdot\boldsymbol{\delta}_{i'j'}^{ij}\big)-\sin^2\big(\boldsymbol{q}\cdot\boldsymbol{\delta}_{i'j'}^{ij}\big)\big\},
\end{aligned} \tag{B7}$$

$$\begin{aligned}
\mathcal{J}_{\boldsymbol{k}} = K\big\{&2\cos\big(\boldsymbol{k}\cdot\boldsymbol{\delta}_{i+1,j+1}^{ij}\big)\\
&-\cos\big(\boldsymbol{k}\cdot\boldsymbol{\delta}_{i+1,j}^{ij}\big)\cos\big(\boldsymbol{q}\cdot\boldsymbol{\delta}_{i+1,j}^{ij}\big)\\
&-\cos\big(\boldsymbol{k}\cdot\boldsymbol{\delta}_{i,j+1}^{ij}\big)\cos\big(\boldsymbol{q}\cdot\boldsymbol{\delta}_{i,j+1}^{ij}\big)\big\}.
\end{aligned} \tag{B8}$$

The expressions presented in this Appendix can be applied to the ferromagnetic phase as well by taking the modulation vector $\boldsymbol{q} = 0$.

APPENDIX C: SUMMARY OF THE HELIMAGNETIC GROUND STATES

In this section, we summarize the helimagnetic ground states obtained from previous experimental and theoretical

TABLE I. Summary of the helimagnetic ground states in $\mathrm{NiI_2}$. Here, we show the results in previous experimental (Expt.) and theoretical (Theor.) works including the system, the obtained spiral phase and the used spin models in the theoretical works. In the spin models, the intralayer exchange J are all considered up to the third-nearest neighbor J_3. In the last line, we show the phase derived in the current work at $J_3 = -0.45J_1$ from J-B-K model.

References	Expt./Theor.	System	Spiral phase	Spin model
Ref. [48]	Expt.	Bilayer ($\mathrm{SiO_2/Si}$ substrate)	IC	–
Ref. [49]	Expt.	Monolayer (hBN substrate)	IC	–
Ref. [50]	Theor.	Bulk	$\mathrm{PS_{cant}}$ (within a single layer)	J-B-K model
Ref. [51]	Theor.	From bulk to monolayer	$\mathrm{PS_{cant}}$ (from bulk to bilayer) IC (monolayer)	J-B-K-A_z model
Ref. [52]	Theor.	Monolayer	IC	J-K model
Ref. [53]	Theor.	Monolayer	IC (noncoplanar)	J-K model
Ref. [54]	Expt.	Bulk	$\mathrm{PS_{cant}}$	–
Ref. [57]	Expt.	Bulk	$\mathrm{PS_{cant}}$	–
Ref. [60]	Expt.	Monolayer (HOPG substrate)	IM	–
Ref. [61]	Expt.	Monolayer (graphene-covered SiC substrate)	IC (with canting spin rotation plane)	–
Current work	Theor.	A single-layer within few-layer $\mathrm{NiI_2}$	IM	J-B-K model

works in $\mathrm{NiI_2}$, as listed in Table I. For comparison, we also include our analytical results in the last line of the table, where the parameters are adopted to be the same as those in Ref. [50] with $J_3 = -0.45J_1$.

---

[1] K. S. Novoselov, A. K. Geim, S. V. Morozov, D. Jiang, Y. Zhang, S. V. Dubonos, I. V. Grigorieva, and A. A. Firsov, Electric field effect in atomically thin carbon films, Science **306**, 666 (2004).

[2] S. Z. Butler, S. M. Hollen, L. Cao, Y. Cui, J. A. Gupta, H. R. Gutiérrez, T. F. Heinz, S. S. Hong, J. Huang, A. F. Ismach *et al.*, Progress, challenges, and opportunities in two-dimensional materials beyond graphene, ACS Nano **7**, 2898 (2013).

[3] G. Fiori, F. Bonaccorso, G. Iannaccone, T. Palacios, D. Neumaier, A. Seabaugh, S. K. Banerjee, and L. Colombo, Electronics based on two-dimensional materials, Nature Nanotechnol. **9**, 768 (2014).

[4] C. Tan, X. Cao, X.-J. Wu, Q. He, J. Yang, X. Zhang, J. Chen, W. Zhao, S. Han, G.-H. Nam *et al.*, Recent advances in ultrathin two-dimensional nanomaterials, Chem. Rev. **117**, 6225 (2017).

[5] X. Zheng, S. Chen, J. Li, H. Wu, C. Zhang, D. Zhang, X. Chen, Y. Gao, F. He, L. Hui *et al.*, Two-dimensional carbon graphdiyne: Advances in fundamental and application research, ACS Nano **17**, 14309 (2023).

[6] H. Zhou, S. Li, K.-W. Ang, and Y.-W. Zhang, Recent advances in in-memory computing: Exploring memristor and memtransistor arrays with 2D materials, Nano-Micro Lett. **16**, 121 (2024).

[7] R. Rani and M. M. Sinha, Recent advances in two-dimensional transition metal oxides and di-chalcogenides as efficient thermoelectric materials, Phys. Scr. **99**, 032002 (2024).

[8] B. Radisavljevic, A. Radenovic, J. Brivio, V. Giacometti, and A. Kis, Single-layer $\mathrm{MoS_2}$ transistors, Nature Nanotechnol. **6**, 147 (2011).

[9] A. A. Balandin, S. Ghosh, W. Bao, I. Calizo, D. Teweldebrhan, F. Miao, and C. N. Lau, Superior thermal conductivity of single-layer graphene, Nano Lett. **8**, 902 (2008).

[10] C. Wang, J. Guo, L. Dong, A. Aiyiti, X. Xu, and B. Li, Superior thermal conductivity in suspended bilayer hexagonal boron nitride, Sci. Rep. **6**, 25334 (2016).

[11] R. R. Nair, P. Blake, A. N. Grigorenko, K. S. Novoselov, T. J. Booth, T. Stauber, N. M. R. Peres, and A. K. Geim, Fine structure constant defines visual transparency of graphene, Science **320**, 1308 (2008).

[12] L. Song, L. Ci, H. Lu, P. B. Sorokin, C. Jin, J. Ni, A. G. Kvashnin, D. G. Kvashnin, J. Lou, B. I. Yakobson *et al.*, Large scale growth and characterization of atomic hexagonal boron nitride layers, Nano Lett. **10**, 3209 (2010).

[13] Z. Yin, H. Li, H. Li, L. Jiang, Y. Shi, Y. Sun, G. Lu, Q. Zhang, X. Chen, and H. Zhang, Single-layer $\mathrm{MoS_2}$ phototransistors, ACS Nano **6**, 74 (2012).

[14] B. Huang, G. Clark, E. Navarro-Moratalla, D. R. Klein, R. Cheng, K. L. Seyler, D. Zhong, E. Schmidgall, M. A. McGuire, D. H. Cobden *et al.*, Layer-dependent ferromagnetism in a van der Waals crystal down to the monolayer limit, Nature (London) **546**, 270 (2017).

[15] C. Gong, L. Li, Z. Li, H. Ji, A. Stern, Y. Xia, T. Cao, W. Bao, C. Wang, Y. Wang *et al.*, Discovery of intrinsic ferromagnetism in two-dimensional van der Waals crystals, Nature (London) **546**, 265 (2017).

[16] S. Jiang, L. Li, Z. Wang, K. F. Mak, and J. Shan, Controlling magnetism in 2D $\mathrm{CrI_3}$ by electrostatic doping, Nature Nanotechnol. **13**, 549 (2018).

[17] H. Wang, J. Qi, and X. Qian, Electrically tunable high Curie temperature two-dimensional ferromagnetism in van der Waals layered crystals, Appl. Phys. Lett. **117**, 083102 (2020).

[18] B. Huang, G. Clark, D. R. Klein, D. MacNeill, E. Navarro-Moratalla, K. L. Seyler, N. Wilson, M. A. McGuire, D. H. Cobden, D. Xiao *et al.*, Electrical control of 2D magnetism in bilayer $\mathrm{CrI_3}$, Nature Nanotechnol. **13**, 544 (2018).

[19] N. C. Frey, A. Bandyopadhyay, H. Kumar, B. Anasori, Y. Gogotsi, and V. B. Shenoy, Surface-engineered MXenes: Electric field control of magnetism and enhanced magnetic anisotropy, ACS Nano **13**, 2831 (2019).

[20] A. Edström, D. Amoroso, S. Picozzi, P. Barone, and M. Stengel, Curved magnetism in $\mathrm{CrI_3}$, Phys. Rev. Lett. **128**, 177202 (2022).

[21] C. Wang, L. You, D. Cobden, and J. Wang, Towards two-dimensional van der Waals ferroelectrics, Nature Mater. **22**, 542 (2023).

[22] S. Lin, G. Zhang, Q. Lai, J. Fu, W. Zhu, and H. Zeng, Recent advances in layered two-dimensional ferroelectrics from material to device, Adv. Funct. Mater. **33**, 2304139 (2023).

[23] S. Wan, Y. Li, W. Li, X. Mao, C. Wang, C. Chen, J. Dong, A. Nie, J. Xiang, Z. Liu *et al.*, Nonvolatile ferroelectric memory effect in ultrathin α-$\mathrm{In_2Se_3}$, Adv. Funct. Mater. **29**, 1808606 (2019).

[24] W. Huang, F. Wang, L. Yin, R. Cheng, Z. Wang, M. G. Sendeku, J. Wang, N. Li, Y. Yao, and J. He, Gate-coupling-enabled robust hysteresis for nonvolatile memory and programmable rectifier in Van der Waals ferroelectric heterojunctions, Adv. Mater. **32**, 1908040 (2020).

[25] J. Xiao, Y. Wang, H. Wang, C. D. Pemmaraju, S. Wang, P. Muscher, E. J. Sie, C. M. Nyby, T. P. Devereaux, X. Qian *et al.*, Berry curvature memory through electrically driven stacking transitions, Nature Phys. **16**, 1028 (2020).

[26] H. Schmid, Multi-ferroic magnetoelectrics, Ferroelectrics **162**, 317 (1994).

[27] K. Shen, Magnon-ferron coupling mediated by dynamical Dzyaloshinskii-Moriya interaction in a two-dimensional multiferroic model, Phys. Rev. B **106**, 104411 (2022).

[28] K. Shen, Electrical and magnetic control of spin-lattice configuration and magnon-ferron hybridization in a two-dimensional multiferroic model, Phys. Rev. B **108**, 094413 (2023).

[29] G. A. Smolenskii, V. A. Isupov, N. N. Krainik, and A. I. Agranovskaya, The coexistence of the ferroelectric and ferromagnetic states, Izv. Akad. Nauk SSSR Ser. Fiz. **25**, 1333 (1961).

[30] J.-M. Liu and C.-W. Nan, Decade of multiferroic researches, Physics **43**, 88 (2014).

[31] N. A. Spaldin and R. Ramesh, Advances in magnetoelectric multiferroics, Nature Mater. **18**, 203 (2019).

[32] J. Wang, J. B. Neaton, H. Zheng, V. Nagarajan, S. B. Ogale, B. Liu, D. Viehland, V. Vaithyanathan, D. G. Schlom, U. V. Waghmare *et al.*, Epitaxial $\mathrm{BiFeO_3}$ multiferroic thin film heterostructures, Science **299**, 1719 (2003).

[33] V. V. Shvartsman, W. Kleemann, R. Haumont, and J. Kreisel, Large bulk polarization and regular domain structure in ceramic $\mathrm{BiFeO_3}$, Appl. Phys. Lett. **90**, 172115 (2007).

[34] D. Lebeugle, D. Colson, A. Forget, M. Viret, P. Bonville, J. F. Marucco, and S. Fusil, Room-temperature coexistence of large electric polarization and magnetic order in $\mathrm{BiFeO_3}$ single crystals, Phys. Rev. B **76**, 024116 (2007).

[35] G. Catalan and J. F. Scott, Physics and applications of bismuth ferrite, Adv. Mater. **21**, 2463 (2009).

[36] T. Kimura, S. Kawamoto, I. Yamada, M. Azuma, M. Takano, and Y. Tokura, Magnetocapacitance effect in multiferroic $\mathrm{BiMnO_3}$, Phys. Rev. B **67**, 180401(R) (2003).

[37] Y. Yang, J.-M. Liu, H. B. Huang, W. Q. Zou, P. Bao, and Z. G. Liu, Magnetoelectric coupling in ferroelectromagnet $\mathrm{Pb(Fe_{1/2}Nb_{1/2})O_3}$ single crystals, Phys. Rev. B **70**, 132101 (2004).

[38] O. Raymond, R. Font, N. Suárez-Almodovar, J. Portelles, and J. M. Siqueiros, Frequency-temperature response of ferroelectromagnetic $\mathrm{Pb(Fe_{1/2}Nb_{1/2})O_3}$ ceramics obtained by different precursors. Part I. Structural and thermo-electrical characterization, J. Appl. Phys. **97**, 084107 (2005).

[39] T. Kimura, T. Goto, H. Shintani, K. Ishizaka, T. Arima, and Y. Tokura, Magnetic control of ferroelectric polarization, Nature (London) **426**, 55 (2003).

[40] T. Kimura, S. Ishihara, H. Shintani, T. Arima, K. T. Takahashi, K. Ishizaka, and Y. Tokura, Distorted perovskite with e_g^1 configuration as a frustrated spin system, Phys. Rev. B **68**, 060403(R) (2003).

[41] M. Kenzelmann, A. B. Harris, S. Jonas, C. Broholm, J. Schefer, S. B. Kim, C. L. Zhang, S.-W. Cheong, O. P. Vajk, and J. W. Lynn, Magnetic inversion symmetry breaking and ferroelectricity in $\mathrm{TbMnO_3}$, Phys. Rev. Lett. **95**, 087206 (2005).

[42] T. Aoyama, K. Yamauchi, A. Iyama, S. Picozzi, K. Shimizu, and T. Kimura, Giant spin-driven ferroelectric polarization in $\mathrm{TbMnO_3}$ under high pressure, Nature Commun. **5**, 4927 (2014).

[43] H. Katsura, N. Nagaosa, and A. V. Balatsky, Spin current and magnetoelectric effect in noncollinear magnets, Phys. Rev. Lett. **95**, 057205 (2005).

[44] M. Mostovoy, Ferroelectricity in spiral magnets, Phys. Rev. Lett. **96**, 067601 (2006).

[45] C. Jia, S. Onoda, N. Nagaosa, and J. H. Han, Microscopic theory of spin-polarization coupling in multiferroic transition metal oxides, Phys. Rev. B **76**, 144424 (2007).

[46] T.-H. Arima, Ferroelectricity induced by proper-screw type magnetic order, J. Phys. Soc. Jpn. **76**, 073702 (2007).

[47] Y. J. Choi, H. T. Yi, S. Lee, Q. Huang, V. Kiryukhin, and S.-W. Cheong, Ferroelectricity in an Ising chain magnet, Phys. Rev. Lett. **100**, 047601 (2008).

[48] H. Ju, Y. Lee, K.-T. Kim, I. H. Choi, C. J. Roh, S. Son, P. Park, J. H. Kim, T. S. Jung, J. H. Kim *et al.*, Possible persistence of multiferroic order down to bilayer limit of van der Waals material $\mathrm{NiI_2}$, Nano Lett. **21**, 5126 (2021).

[49] Q. Song, C. A. Occhialini, E. Ergeçen, B. Ilyas, D. Amoroso, P. Barone, J. Kapeghian, K. Watanabe, T. Taniguchi, A. S. Botana *et al.*, Evidence for a single-layer van der Waals multiferroic, Nature (London) **602**, 601 (2022).

[50] X. Li, C. Xu, B. Liu, X. Li, L. Bellaiche, and H. Xiang, Realistic spin model for multiferroic $\mathrm{NiI_2}$, Phys. Rev. Lett. **131**, 036701 (2023).

[51] N. Liu, C. Wang, C. Yan, C. Xu, J. Hu, Y. Zhang, and W. Ji, Competing multiferroic phases in monolayer and few-layer NiI_2, Phys. Rev. B **109**, 195422 (2024).

[52] J. Sødequist and T. Olsen, Type II multiferroic order in two-dimensional transition metal halides from first principles spin-spiral calculations, 2D Mater. **10**, 035016 (2023).

[53] D. Amoroso, P. Barone, and S. Picozzi, Spontaneous skyrmionic lattice from anisotropic symmetric exchange in a Ni-halide monolayer, Nature Commun. **11**, 5784 (2020).

[54] T. Kurumaji, S. Seki, S. Ishiwata, H. Murakawa, Y. Kaneko, and Y. Tokura, Magnetoelectric responses induced by domain rearrangement and spin structural change in triangular-lattice helimagnets NiI_2 and CoI_2, Phys. Rev. B **87**, 014429 (2013).

[55] D. Billerey, C. Terrier, N. Ciret, and J. Kleinclauss, Neutron diffraction study and specific heat of antiferromagnetic NiI_2, Phys. Lett. A **61**, 138 (1977).

[56] D. Billerey, C. Terrier, R. Mainard, and A. J. Pointon, Magnetic phase transition in anhydrous NiI_2, Phys. Lett. A **77**, 59 (1980).

[57] S. R. Kuindersma, J. P. Sanchez, and C. Haas, Magnetic and structural investigations on NiI_2 and CoI_2, Physica B+C **111**, 231 (1981).

[58] C. A. Occhialini, L. G. P. Martins, Q. Song, J. S. Smith, J. Kapeghian, D. Amoroso, J. J. Sanchez, P. Barone, B. Dupé, M. J. Verstraete *et al.*, Signatures of pressure-enhanced helimagnetic order in van der Waals multiferroic NiI_2, arXiv:2306.11720.

[59] Y. Wu, H. Lu, X. Han, C. Yang, N. Liu, X. Zhao, L. Qiao, W. Ji, R. Che, L. Deng *et al.*, Observation of unconventional van der Waals multiferroics near room temperature, arXiv:2311.14300.

[60] M. Amini, A. O. Fumega, H. González-Herrero, V. Vaňo, S. Kezilebieke, J. L. Lado, and P. Liljeroth, Atomic-scale visualization of multiferroicity in monolayer NiI_2, Adv. Mater. **36**, 2311342 (2024).

[61] M.-P. Miao, N. Liu, W.-H. Zhang, D.-B. Wang, W. Ji, and Y.-S. Fu, Spin-resolved imaging of atomic-scale helimagnetism in monolayer NiI_2, arXiv:2309.16526.

[62] J. P. Perdew, K. Burke, and M. Ernzerhof, Generalized gradient approximation made simple, Phys. Rev. Lett. **77**, 3865 (1996).

[63] A. V. Krukau, O. A. Vydrov, A. F. Izmaylov, and G. E. Scuseria, Influence of the exchange screening parameter on the performance of screened hybrid functionals, J. Chem. Phys. **125**, 224106 (2006).

[64] K. Li, S.-L. Yu, and J.-X. Li, Global phase diagram, possible chiral spin liquid, and topological superconductivity in the triangular Kitaev–Heisenberg model, New J. Phys. **17**, 043032 (2015).

[65] T. Holstein and H. Primakoff, Field dependence of the intrinsic domain magnetization of a ferromagnet, Phys. Rev. **58**, 1098 (1940).

[66] R. Shindou, R. Matsumoto, S. Murakami, and J.-I. Ohe, Topological chiral magnonic edge mode in a magnonic crystal, Phys. Rev. B **87**, 174427 (2013).

[67] K. Shen, Magnon spin transport around the compensation magnetic field in easy-plane antiferromagnetic insulators, J. Appl. Phys. **129**, 223906 (2021).

[68] K. Shen, Finite temperature magnon spectra in yttrium iron garnet from a mean field approach in a tight-binding model, New J. Phys. **20**, 043025 (2018).

[69] N. D. Mermin and H. Wagner, Absence of ferromagnetism or antiferromagnetism in one- or two-dimensional isotropic Heisenberg models, Phys. Rev. Lett. **17**, 1133 (1966).

[70] K. Shen, Temperature-switched anomaly in the spin Seebeck effect in $\mathrm{Gd}_3\mathrm{Fe}_5\mathrm{O}_{12}$, Phys. Rev. B **99**, 024417 (2019).

[71] S. Toth and B. Lake, Linear spin wave theory for single-Q incommensurate magnetic structures, J. Phys.: Condens. Matter **27**, 166002 (2015).

[72] B. Flebus, K. Shen, T. Kikkawa, K.-i. Uchida, Z. Qiu, E. Saitoh, R. A. Duine, and G. E. W. Bauer, Magnon-polaron transport in magnetic insulators, Phys. Rev. B **95**, 144420 (2017).

[73] A. Cong, J. Liu, W. Xue, H. Liu, Y. Liu, and K. Shen, Exchange-mediated magnon-phonon scattering in monolayer CrI_3, Phys. Rev. B **106**, 214424 (2022).

[74] P. Park, K. Park, T. Kim, Y. Kousaka, K. H. Lee, T. G. Perring, J. Jeong, U. Stuhr, J. Akimitsu, M. Kenzelmann *et al.*, Momentum-dependent magnon lifetime in the metallic noncollinear triangular antiferromagnet CrB_2, Phys. Rev. Lett. **125**, 027202 (2020).

[75] Y. Tserkovnyak, A. Brataas, and G. E. W. Bauer, Enhanced gilbert damping in thin ferromagnetic films, Phys. Rev. Lett. **88**, 117601 (2002).

[76] N. N. Orlova, A. A. Avakyants, A. V. Timonina, N. N. Kolesnikov, and E. V. Deviatov, Ferromagnetic response of thin NiI_2 flakes up to room temperatures, arXiv:2309.08392.

[77] S. O. Demokritov, V. E. Demidov, O. Dzyapko, G. A. Melkov, A. A. Serga, B. Hillebrands, and A. N. Slavin, Bose-Einstein condensation of quasi-equilibrium magnons at room temperature under pumping, Nature (London) **443**, 430 (2006).

[78] A. A. Serga, V. S. Tiberkevich, C. W. Sandweg, V. I. Vasyuchka, D. A. Bozhko, A. V. Chumak, T. Neumann, B. Obry, G. A. Melkov, A. N. Slavin *et al.*, Bose-Einstein condensation in an ultra-hot gas of pumped magnons, Nature Commun. **5**, 3452 (2014).

[79] D. A. Bozhko, A. A. Serga, P. Clausen, V. I. Vasyuchka, F. Heussner, G. A. Melkov, A. Pomyalov, V. S. L'vov, and B. Hillebrands, Supercurrent in a room-temperature Bose-Einstein magnon condensate, Nature Phys. **12**, 1057 (2016).

[80] R. Labouvie, B. Santra, S. Heun, S. Wimberger, and H. Ott, Negative differential conductivity in an interacting quantum gas, Phys. Rev. Lett. **115**, 050601 (2015).

[81] G. He, J. Nathawat, C.-P. Kwan, H. Ramamoorthy, R. Somphonsane, M. Zhao, K. Ghosh, U. Singisetti, N. Perea-López, C. Zhou *et al.*, Negative differential conductance & hot-carrier avalanching in monolayer WS2 FETs, Sci. Rep. **7**, 11256 (2017).

[82] Y. Kasahara, K. Sugii, T. Ohnishi, M. Shimozawa, M. Yamashita, N. Kurita, H. Tanaka, J. Nasu, Y. Motome, T. Shibauchi *et al.*, Unusual thermal hall effect in a Kitaev spin liquid candidate $\alpha-\mathrm{RuCl}_3$, Phys. Rev. Lett. **120**, 217205 (2018).

[83] K. Li, Thermal Hall conductivity with sign change in the Heisenberg–Kitaev kagome magnet, Commun. Theor. Phys. **75**, 015702 (2023).

[84] C. Xu, J. Feng, H. Xiang, and L. Bellaiche, Interplay between Kitaev interaction and single ion anisotropy in ferromagnetic CrI_3 and CrGeTe_3 monolayers, npj Comput. Mater. **4**, 57 (2018).